Sparse Filtered SIRT for Electron Tomography

Chen Mu[a], Chiwoo Park[b,*]

[a] *PhD Student, Department of Industrial and Manufacturing Engineering, Florida State University, 2525 Pottsdamer St. Tallahassee, FL 32310*
[b] *Associate Professor, Department of Industrial and Manufacturing Engineering, Florida State University, 2525 Pottsdamer St. Tallahassee, FL 32310*

Abstract

Electron tomographic reconstruction is a method for obtaining a three-dimensional image of a specimen with a series of two dimensional microscope images taken from different viewing angles. Filtered backprojection, one of the most popular tomographic reconstruction methods, does not work well under the existence of image noises and missing wedges. This paper presents a new approach to largely mitigate the effect of noises and missing wedges. We propose a novel filtered backprojection that optimizes the filter of the backprojection operator in terms of a reconstruction error. This data-dependent filter adaptively chooses the spectral domains of signals and noises, suppressing the noise frequency bands, so it is very effective in denoising. We also propose the new filtered backprojection embedded within the simultaneous iterative reconstruction iteration for mitigating the effect of missing wedges. Our numerical study is presented to show the performance gain of the proposed approach over the state-of-the-art.

Keywords: Tomographic Reconstruction, Filtered Backprojection, Filter Optimization, Filtered Backprojection within SIRT

*Corresponding author: Tel.: +1-850-410-6457; fax: +1-850-410-6342;
Email address: cpark5@fsu.edu (Chiwoo Park)

1. Introduction

Electron tomographic reconstruction is a method for reconstructing detailed three-dimensional structures of a specimen with a series of two-dimensional transmission electron microscope images of the specimen from different viewing angles, which has been widely used in materials science and biological science [1]. In practice, a sample stage containing a specimen is tilted around a single axis, and the 2D electron microscope images (*sinograms*) of the specimen are taken for a range of tilt angles with constant intervals. The 3D reconstruction of the specimen (*tomogram*) can be achieved by combining the 2D projection images using a computerized tomographic reconstruction algorithm. There are two factors that determine the quality of the reconstruction: (1) the range and interval of tilt angles, and (2) the signal-to-noise ratio (SNR) of sinograms. Due to instrumentation limitation or specimen thickness, the range of the tilt angles is typically limited to $[-65, 65]$ to $[-75, 75]$ degrees, which creates a "missing wedge" of information. Reconstruction with the missing wedge typically leaves image artifacts in the reconstruction outcome. In addition, when the signal-to-noise ratio of sinograms is low, the reconstruction outcome could be very noisy. This paper is concerned with improving the accuracy and computational efficiency of electron tomographic reconstruction under those limiting factors.

1.1. Past Works

Past works in tomographic reconstruction are largely categorized into two studies, analytical methods and algebraic methods. Analytical methods are based on a continuous representation of the inverse Radon transform using the Central Slice Theorem [2] and the computation of the discrete version of the continuous representation. A popular analytical method is the filtered backprojection or shortly FBP [3]. The FBP is computationally efficient and simple to implement, but it does not work well under a low signal-to-noise

(SNR) ratio of input sinograms. The low SNR value is quite common in practice [4], and the FBP typically produces a very noisy reconstruction with low SNR sinograms. A quick remedy of this issue is to change the filter function in FBP with a low-pass filter such as Cosine or Hann filter. In addition to the issue, FBP suffers from the missing wedge effects when sinograms are available for only limited tilt angles.

Algebraic methods formulate a system of linear equations relating sinograms to the reconstruction outcome and solve the linear equations using an iterative approach, iteratively updating its solution so that it minimizes the mean squared difference between the left and right hand sides of the equations. Depending on their modeling and iterative steps, there are many variants, including the algebraic reconstruction technique [5, ART], the simultaneous iterative reconstruction technique [6, 2, SIRT] and the simultaneous algebraic reconstruction technique [7, SART]. In some literature, the squared difference criterion of the iterative optimization in the algebraic methods was modified to incorporate certain regularization terms such as the total variation regularization [8], the Tikhonov regularization [9, 10] and edge-preserving regularization [11], and it has been numerically shown that the regularizations can improve the reconstruction quality. In general, the algebraic methods perform better than the analytical methods for the cases with limited tilt angles, but these advantages come with the expense of higher computational costs. The cost per iteration increases quadratically with the size and number of input sinograms, and the slow convergence of the iterative approach requires many of those expensive iterations. There are some more efficient approaches that implement algebraic methods by using graphic processing units (GPUs) [12, 13]. In addition, the number of the iterations in the algebraic approaches is a tuning parameter, which typically determines how much detailed features are included in the resulting reconstruction; a too large choice would give a noisy reconstruction, and a too small choice would not give a reconstruction with many missing details. The tuning parameter is generally difficult to determine.

Some improvements of the FBP were sought for better dealing with measurement noises and the missing wedge issue, taking the computational advantages of FBP. The simplest approach is the denoising-and-backprojection approach, which applies denoising filters on projection data before the backprojection is performed [14]. Karimi et. al. [15] proposed an improved patch-based denoising algorithm, and a penalized weighted least-squares investigation is made in sinogram denoising for low dose X-ray [16]. These simple ideas have shown better performance over the FBP for reconstructing with noise sinograms.

More recent approaches tried to optimize the filter in FBP with a certain optimization criterion that was originally proposed and used for the algebraic methods. By doing so, the performance improvement of FBP to the accuracy comparable to the algebraic methods was sought. In this paper, we refer those methods as a filter-optimization approach. Zeng [17] compared the algebraic and FBP approaches, showing that each iteration of the algebraic methods can be seen as 'first backprojecting data and filtering the backprojected images with a ramp filter,' and it is equivalent to 'first filtering and then backprojecting the filtered data.' The finding became the basis to define a novel FBP that behaves similarly as the algebraic method. Some variants of the approaches [18, 19] were proposed. The major benefits of these approaches are that they are just as fast as the original FBP, while their outcomes are comparable to those of the analytical approaches. The major drawback of the approaches is that the methods come with a tuning parameter k that is related to the degree of denoising, which is typically pre-fixed using the rule of thumb without considering the actual noise-level in data. Pelt proposed a data-pendent FBP that optimizes the FBP filter more adaptively to input data and its noise level [20, 21], but the approach still requires multiple iterations to optimize the filter. Therefore, the approach does not have much computational gain over the algebraic approaches. Since in a real (cryo-)electron microscopy setting, the projections are typically gray-level images, some methodologies on the binary

tomographic reconstruction are also proposed. They typically use some shape information based regularization term combined with energy-minimization [22], or a cost optimization by the simulated annealing algorithm [23]. The second method also jointly solves reconstruction and projection direction assignment for unknown directions of projections.

In considering the missing wedge issue, some recent approaches focus on the utilization of the moment concept and the relations among moments of projections or moments of images in reconstruction [24, 25, 26]. Those methods build the relationships above in order to estimate the unknown projections from the computed image moments for the missing wedge issue, where the reconstruction can be done by approximate inverse moment transform. Different moments such as orthogonal moments [25] and Tchebichef moments [26] can be used and in which Tchebichef moments show a better image representation capability.

1.2. Contributions

We propose a new filter-optimization approach and its embedding within SIRT iterations. We first formulate a new optimization problem of optimizing the filter in FBP with the objective function that comprises a reconstruction accuracy term and a regularization term. The regularization term is the sparsity regularization in a frequency domain to suppress the noisy frequency bands of input sinogram data, and the weighting on the regularization term is determined adaptively to the noise level of the sinogram data. Therefore, the new approach produces a data-dependent filter like Pelt's [21], but the proposed approach does not require any computationally expensive iterations to optimize the filter. Therefore, the proposed approach has computational benefit over the existing data-dependent filters, while maintaining its reconstruction accuracy. We also propose the embedding of the new filter optimization approach with SIRT iterations, replacing the backprojection operator in the SIRT iterations with the new filtered backprojection, which further improves the reconstruction accuracy and reduces missing wedge effects. The integrated algorithm converges

significantly faster than the SIRT iterations, because the regularization term in our filter optimization regularizes the sequence of solution updates so draws a faster convergence of the iterations. To sum up, we are proposing two novel approaches: a new filter-optimization approach and its integration with the SIRT. The filter-optimization approach is referred to as the data-dependent sparse filtered backprojection (sFBP), and its integration into the SIRT is referred to as the sparse filtered SIRT (sfSIRT).

1.3. Organization of This Paper

The remainder of this paper is organized as follows. Section 2 describes the sFBP with its numerical comparison to the state-of-the-art for noisy sinograms. Section 3 describes the sfSIRT with its numerical comparison to existing iterative construction approaches for limited tilt series. Section 4 presents the 3D reconstruction examples using experimental tomography data. Finally we have conclusions in Section 5.

2. Sparse Filtered Backprojection (sFBP)

In electron tomography, an object of interest in a (x, y, z)-space is placed on a sample stage of an electron microscope. The sample stage is rotated around a tilt axis z, and an electron beam irradiates the sample stage in the direction parallel to the (x, y)-plane. Detecting the electron beam going through the sample produces the 2D projection images of the object for different tile angles, which are referred to as a sinogram. The object of interest can be represented as a stack of its 2D parallel slices along the z-direction, and each of the 2D slices can be reconstructed independently using the corresponding slice of sinogram [27]. In this section, we describe our new filter backprojection approach to reconstruct each 2D slice. Since the z coordinate is fixed for the reconstruction, we omit the z coordinate in describing our approach for simpler notations.

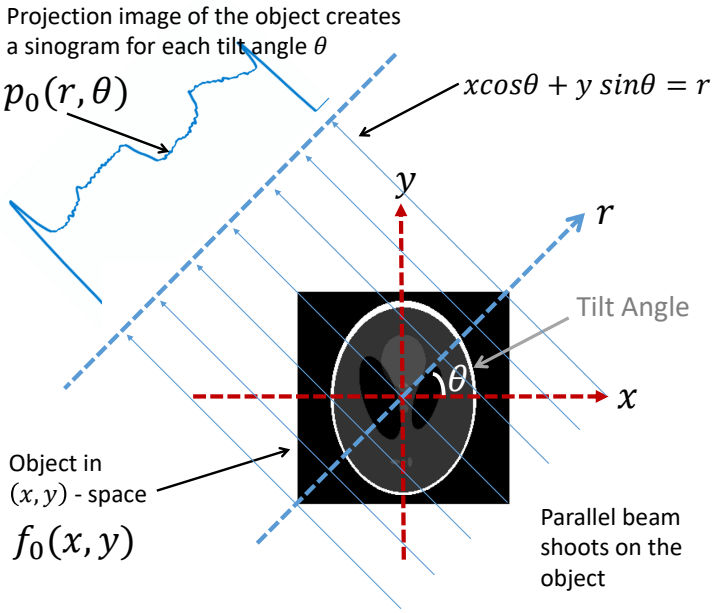

Figure 1: Principle of a parallel beam projection. A detector measures an integral of the object image in along the line characterized by $x\cos\theta + y\sin\theta = r$.

To describe a general tomographic imaging and explain our proposed idea for tomographic reconstruction, we first introduce a few notations. Let $f_0(x,y)$ denote an unknown object image of interest in (x,y)-space. Let $\mathcal{R}\circ f_0(r,\theta)$ denote the line integral of the image over the line characterized by $x\cos\theta + y\sin\theta = r$,

$$\mathcal{R}\circ f_0(r,\theta) = \int_{-\infty}^{\infty}\int_{-\infty}^{\infty} f_0(x,y)\delta(x\cos\theta + y\sin\theta - r)\mathrm{d}x\mathrm{d}y. \qquad (1)$$

As shown in Figure 1, the line represents an electron irradiation ray, and the line integration represents the sum of all object image intensities along the line. When there is no measurement noise, the line integrals for different values of projection dimension r and rotation θ are measured in tomography, which are referred to as *sinogram*. We denote the non-noisy sinogram by $p_0(r,\theta)$. Tomographic reconstruction is to recover $f_0(x,y)$ from the sinogram $p_0(r,\theta)$ or more often its noisy version.

For the tomographic reconstruction, our sparsity-regularized FBP (sFBP) work in the Fourier feature of the sinogram. Let $\mathcal{F}_2 \circ f_0(u,v)$ denote the 2-D Fourier transform of $f_0(x,y)$. $f_0(x,y)$ is the inverse Fourier transform of $\mathcal{F}_2 \circ f_0(u,v)$,

$$f_0(x,y) = \int_{-\infty}^{\infty}\int_{-\infty}^{\infty} \mathcal{F}_2 \circ f_0(u,v) e^{j2\pi(ux+vy)} \mathrm{d}u\mathrm{d}v.$$

By the change of variables from (u,v) to (ω,θ) with the relation $u = \omega\cos\theta$ and $v = \omega\sin\theta$, we can rewrite the inverse Fourier transform,

$$f_0(x,y) = \int_{0}^{\pi}\int_{-\infty}^{\infty} q(\omega,\theta)|\omega| e^{j2\pi w(x\cos\theta + y\sin\theta)} \mathrm{d}\omega\mathrm{d}\theta, \tag{2}$$

where $q(\omega,\theta) = \mathcal{F}_2 \circ f_0(\omega\cos\theta, \omega\sin\theta)$. The central slice theorem [2] basically reads

$$q(\omega,\theta) = \mathcal{F}_1 \circ p_0(\omega,\theta),$$

where $\mathcal{F}_1 \circ p_0(\omega,\theta)$ is the 1-D Fourier transform of the sinogram $p_0(r,\theta)$ with respect to the first input dimension r. Replacing the term $q(\omega,\theta)$ in equation (2) with $\mathcal{F}_1 \circ p_0(\omega,\theta)$, the equation becomes

$$f_0(x,y) = \int_{-\infty}^{\infty}\int_{0}^{\pi} \mathcal{F}_1 \circ p_0(\omega,\theta)|\omega| e^{j2\pi w(x\cos\theta + y\sin\theta)} \mathrm{d}\theta\mathrm{d}\omega.$$

The equation basically relates the non-noisy sinogram $p_0(r,\theta)$ to a real space image $f_0(x,y)$ as

$$f_0(x,y) = \int_{-\infty}^{\infty}\int_{0}^{\pi} Q_{p_0}(\omega;x,y,\theta)|\omega| \mathrm{d}\theta\mathrm{d}\omega.$$

where $Q_{p_0}(\omega;x,y,\theta) = \mathcal{F}_1 \circ p_0(\omega,\theta) e^{j2\pi w(x\cos\theta + y\sin\theta)}$. When the sinogram data are only available at a finite number of locations (ω,θ), so the integration equation is approximated by its finite dimensional version. Let Ω denote a finite number of the ω values and Θ denote a finite set of the θ values. The finite dimensional version is

$$f_0(x,y) \approx \sum_{\omega\in\Omega} \left\{ \sum_{\theta\in\Theta} Q_{p_0}(\omega;x,y,\theta) \right\} |\omega|. \tag{3}$$

This defines the linear problem for the filtered backprojection procedure [2], which is basically the weighted sum of $Q_{p_0}(\omega;x,y,\theta)$ with weight $|\omega|$; the

weight is referred as to the filter of the backprojection, and the specific choice $|\omega|$ is known as the Ram-Lak filter.

In practice, the sinogram data $p_0(r,\theta)$ is corrupted through an additive noise process $\epsilon(r,\theta)$,

$$p(r,\theta) = p_0(r,\theta) + \epsilon(r,\theta). \tag{4}$$

When the filtered backprojection procedure is applied to the noisy version $p(r,\theta)$, the reconstruction outcome becomes

$$\begin{aligned} f(x,y) =& \sum_{\omega\in\Omega}\sum_{\theta\in\Theta} Q_p(\omega;x,y,\theta)|\omega| \\ =& \sum_{\omega\in\Omega}\sum_{\theta\in\Theta} Q_{p_0}(\omega;x,y,\theta)|\omega| + \sum_{\omega\in\Omega}\sum_{\theta\in\Theta} Q_{\epsilon}(\omega;x,y,\theta)|\omega| \\ =& f_0(x,y) + \sum_{\omega\in\Omega}\sum_{\theta\in\Theta} Q_{\epsilon}(\omega;x,y,\theta)|\omega|, \end{aligned} \tag{5}$$

where $Q_\epsilon(\omega;x,y,\theta) = \mathcal{F}_1 \circ \epsilon(\omega,\theta)e^{j2\pi w(x\cos\theta + y\sin\theta)}$ is the effect of observation noise on the reconstructed image $f(x,y)$. Note that the noise effect term, $Q_\epsilon(\omega;x,y,\theta)$, is summed over different frequencies ω. We assume that there are some frequency bands ω with relatively low $Q_\epsilon(\omega;x,y,\theta)$ and relatively high $Q_{p_0}(\omega;x,y,\theta)$; otherwise, noises and true signals are indistinguishable in the Fourier domain. Let W denote this set of the frequency bands. We propose to find W and suppress $Q_\epsilon(\omega;x,y,\theta)$ for $\omega \notin W$ by replacing the filter $|\omega|$ with

$$|\omega|\delta(\omega \in W), W \subset \Omega, \tag{6}$$

where $\delta(\cdot)$ is the Dirac delta function. The modification is valued $|\omega|$ when ω is an element of the subset W and is zero-valued otherwise. The choice of the subset W is important. Ideally, W should exclude the frequency bands dominated by noises. Let $f_W(x,y)$ denote the resulting reconstruction for a choice of W,

$$f_W(x,y) = \sum_{\theta\in\Theta}\sum_{\omega\in\Omega} (\mathcal{F}_1 \circ p(\omega,\theta)\delta(\omega\in W))e^{j2\pi w(x\cos\theta + y\sin\theta)}|\omega|. \tag{7}$$

We optimize the choice of the subset W by minimizing the regularized reconstruction error

$$\begin{aligned} &\text{Minimize} \quad ||f_W - f||_2^2 + \lambda \mathcal{P}(f_W), \\ &\text{subject to} \quad W \subset \Omega, \end{aligned} \tag{8}$$

where $||f||_2^2 := \int\int f^2 dxdy$ is the L2 norm of function f, and $\mathcal{P}(f_W) := |W|$ is the cardinality of W. The optimization criterion basically pursues for minimizing the reconstruction error while using the information from a less number of the frequency bands. When the value of f is only available at a finite number of (x, y)'s, the norm is the sum of the squares of the function values at the finite (x, y) locations. Since the discrete Fourier transform is an orthonormal transformation, the L2 norm of f is equivalent to the sum of the squares of the discrete Fourier coefficients of the function:

$$||f||_2^2 = \sum_{\omega \in \Omega, \theta \in \Theta} |\mathcal{F}_2 \circ f(\omega \cos\theta, \omega \sin\theta)|^2. \tag{9}$$

Please note that the term $|\omega|$ is not shown in the right side of equation (9), because the term is a part of the inverse Fourier transform in the polar coordinates, not the corresponding Fourier coefficients. Since $\mathcal{F}_2 \circ f(\omega \cos\theta, \omega \sin\theta) = \mathcal{F}_1 \circ p(\omega, \theta)$ by the central slice theorem [2], the norm is equivalent to

$$||f||_2^2 = \sum_{\omega \in \Omega, \theta \in \Theta} |\mathcal{F}_1 \circ p(\omega, \theta)|^2. \tag{10}$$

Due to the following results,

$$\begin{aligned} &f_W(x, y) - f(x, y) = \\ &\qquad \sum_{\theta \in \Theta} \sum_{\omega \in \Omega} [\mathcal{F}_1 \circ p(\omega, \theta) \delta(\omega \in W) - \mathcal{F}_1 \circ p(\omega, \theta)] e^{j2\pi w(x\cos\theta + y\sin\theta)} |\omega|, \end{aligned}$$

we have

$$\begin{aligned} ||f_W - f||_2^2 &= \sum_{\omega \in \Omega, \theta \in \Theta} |\mathcal{F}_1 \circ p(\omega, \theta) \delta(\omega \in W) - \mathcal{F}_1 \circ p(\omega, \theta)|^2 \\ &= \sum_{\omega \in \Omega \setminus W} \sum_{\theta \in \Theta} |\mathcal{F}_1 \circ p(\omega, \theta)|^2, \end{aligned} \tag{11}$$

and the optimization problem in equation (8) becomes

$$\begin{aligned} \text{Minimize} \quad & \sum_{\omega\in\Omega\setminus W}\sum_{\theta\in\Theta}|\mathcal{F}_1\circ p(\omega,\theta)|^2+\lambda|W| \\ \text{subject to} \quad & W\subset\Omega. \end{aligned} \tag{12}$$

One can easily show that the optimal solution for the problem is simply the following hard thresholding rule,

$$W^*=\left\{\omega\in\Omega;\sum_{\theta\in\Theta}|\mathcal{F}_1\circ p(\omega,\theta)|^2\geq\lambda\right\}. \tag{13}$$

Applying the optimal choice W^* to the backprojection (7) is led to the new approach, data-dependent sparse filtered backprojection (sFBP), which is described by

$$f_{W^*}(x,y)=\sum_{\theta\in\Theta}\sum_{\omega\in\Omega}(\mathcal{F}_1\circ p(\omega,\theta)\delta(\omega\in W^*))e^{j2\pi w(x\cos\theta+y\sin\theta)}|\omega|. \tag{14}$$

2.1. Tuning parameter λ

The choice of λ in the optimization problem (8) is critical for the performance. Too large λ choices would zero out too many frequency bands so would lead to too much loss in reconstruction details, while too small λ choices would keep significant noise information in tomographic reconstruction. Mainly motivated by the fact that the optimization formulation (8) is a $L1$-penalized regression problem, we considered and tried the existing penalty parameter selection criteria for a L1-penalized regression problem, including Akaike Information Criterion (AIC) [28, 29], Bayesian Information Criterion (BIC) [30], and the generalized model description length (gMDL) model selection criterion [31, 32]. Among the three, gMDL numerically worked best for most of our numerical cases, so we propose to choose λ using gMDL, which chooses the λ that minimizes the following generalization error:

$$\begin{aligned} \text{gMDL}(\lambda)=&\frac{|\Omega|}{2}\log(||f_W-f||_2) \\ &+\frac{|W|}{2}\log\frac{||f_W||_2/|W|}{||f_W-f||_2/(|\Omega|-|W|)}+\log|\Omega|. \end{aligned} \tag{15}$$

The gMDL uses a data driven penalty to the L2-loss in a penalized regression problem, and it overcomes the limitations of the AIC and BIC criteria [31, 32].

2.2. Implementation and Complexity

Suppose that we have noisy sinogram, $p(r,\theta)$, for $r \in \{r_1, r_2, \ldots, r_{N_d}\}$ and $\theta \in \{\theta_1, \theta_2, \ldots, \theta_{N_\theta}\}$. Its 1-D fourier transform with respect to dimension r can be taken for each θ to get

$$\mathcal{F}_1 \circ p(\omega, \theta).$$

According to (13), the solution for the optimization (12) can be achieved by the simple thresholding rule on $\sum_{\theta\in\Theta} |\mathcal{F}_1 \circ p(\omega,\theta)|^2$ with threshold λ, and the possible choices of λ are limited to the possible values of $\sum_{\theta\in\Theta} |\mathcal{F}_1 \circ p(\omega,\theta)|^2$. For λ in the possibles, one can evaluate $gMDL(\lambda)$, and the optimal λ is chosen as one achieving the minimum gMDL. Once λ is chosen, we can simply evaluate the backprojection (14). The computation steps of the sFBP is summarized below:

Input. Discrete projection data $p(r,\theta)$ for $r \in \{r_1, r_2, \ldots, r_{N_d}\}$ and $\theta \in \{\theta_1, \theta_2, \ldots, \theta_{N_\theta}\}$.

Step 1. For each θ_j, take the 1-D Fast Fourier transform of $p(r, \theta = \theta_j)$ and denote the Fourier coefficients by $c(\omega_i, \theta_j) := \mathcal{F}_1 \circ p(\omega_i, \theta_j)$ for $i = 1, ..., N_d$ and $j = 1, ..., N_\theta$.

Step 2. Compute $\alpha_i = \sum_{j=1}^{N_\theta} c(\omega_i, \theta_j)^2$. Compute the order statistics of the α_i's by sorting them. Let $i(k)$ denote the index of the kth largest one among them.

Step 3. Denote $k* = \arg\min_{k=1,\ldots,N_d} gMDL(\lambda = \alpha_{i(k)})$.

Step 4. $\lambda = \alpha_{i(k*)}$ and $W^* = \{\omega_{i(1)}, \omega_{i(2)}, \ldots, \omega_{i(k*)}\}$.

Step 5. Compute f_{W^*} using equation (14).

The computational complexity of Step 1 through Step 4 is dominated by the complexity of Step 1, which is $O(N_\theta N_d \log(N_d))$, because the complexity of the 1D fourier transform for each θ is $O(N_d \log(N_d))$. The complexity of Step 5 is $O(N_\theta N^2)$, where we assumed that the backprojection outcome consists of

$N \times N$ pixels. When $N_d \approx N$, the total computation complexity is $O(N_\theta N^2)$, which is same as the complexity of the standard FBP.

2.3. Numerical Comparison of sFBP to the State-of-the-Art

In this section, we present the numerical performance of sFBP for simulated datasets and compare it with those from some baseline methods and the state-of-the-art. For the baseline methods, we chose the FBP with Ram-Lak Filter or shortly FBP(RL) and the FBP with the Hann filter or shortly FBP(HN) to see the performance gain of our filter optimization approach over the standard FBP approaches. Using the Ram-Lak filter typically magnifies high frequency noises in projection data during its reconstruction procedure, while the Hann filter has some ability in filtering out high-frequency noises. We also included the simultaneous iterative reconstruction technique (SIRT) as another baseline method. The performance of the SIRT depends on the number of iterations. We set the numbers of iterations to either 50 or 100. We use SIRT(k) to represent SIRT with k iterations. For the state-of-the-art methods, we chose one representative from each different approach. The iterative and Landweber filtered backprojection [18, L-FBP] was chosen as a representative of the filter optimization approach, which outperformed other filter optimization approaches in our numerical cases. The generalized Tikhonov regularization reconstruction method [10, TR] was chosen as a representative of an algebraic approach. The sinogram denoising method [33, SMF-FBP] was chosen as a representative of the sinogram denoising approach, which outperformed other similar approaches. We also chose Backprojection Wiener deconvolution [34, BPWD] as an example of backprojction-then-filtering approach. For L-FBP and BPWD, we used the author's Matlab implementation and we implemented all of the other algorithms in Matlab (MathWorks, Inc., MA, USA).

We compare the different approaches in terms of reconstruction accuracy and computation speed under different simulated scenarios. For the comparison, we used four test images as shown in Figure 2, some of which were from the

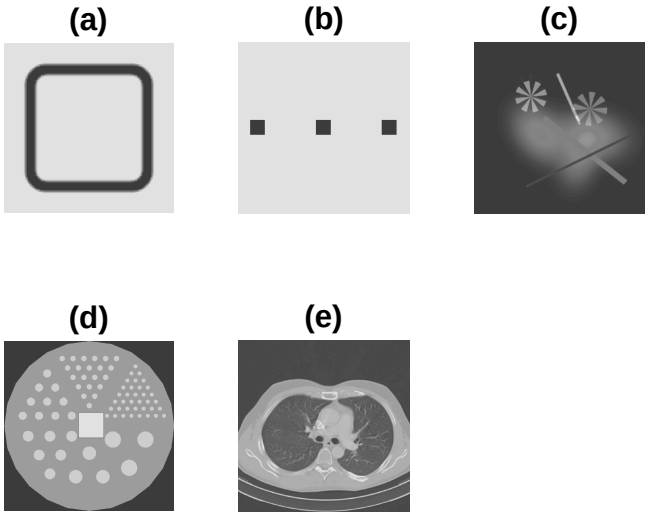

Figure 2: Five test images of (a) box phantom image of size 128×128, (b) three-dot phantom image of size 128×128, (c) phantom-256 image of size 256×256, (d) phantom-520 image size 520×520, (e) CT thorax image of size 512×512. They are all of gray scale.

literature [20, 35]. The sinograms of the four test images were computed using the Radon transform, and the projection data were modified by adding observation noises, before being used in the reconstruction methods. We used Poisson noises, and we varied the Poisson intensity (denoted by P) over 10^3, $10^{5.5}$ and $10^{6.5}$ to simulate different levels of noises.

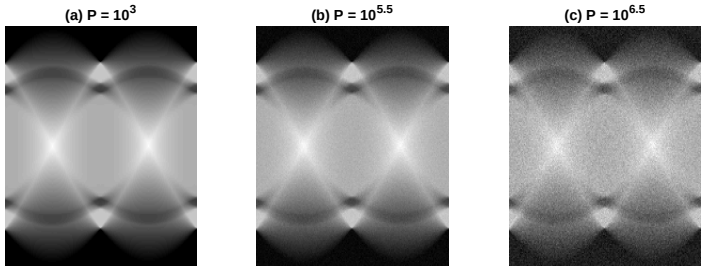

Figure 3: Sinogram with Poisson noises; P is the Poisson intensity.

Figure 3 shows exemplary projection data with different noise intensities applied on the second test image. The noisy sinogram data were used as inputs to each of the compared methods, and the resulting reconstruction $\hat{f}$ was com-

pared with the groundtruth f_0 to evaluate the reconstruction accuracy. We used two accuracy measures popularly used in computational tomography, the peak signal-to-noise ratio (PSNR) and the structural similarity index (SSIM). The PSNR criterion measures the average reconstruction error:

$$PSNR(\hat{f}_0) = 10\log_{10}(f_{0_{MAX}}^2/MSE(\hat{f}_0)),$$

where

$$MSE(\hat{f}_0) = \frac{1}{|X||Y|}\sum_{x\in X}\sum_{y\in Y}(\hat{f}_0(x,y) - f_0(x,y))^2$$

and $f_{0_{MAX}}$ is the max value among all entries of $f_0(x,y)$.

The SSIM [36] is a common criterion to quantify the similarity of reconstruction $\hat{f}_0$ and ground truth f_0 images in terms of image structures and edge-preserving properties, which is defined by

$$SSIM(\hat{f}_0) = [a(f_0,\hat{f}_0)]^\alpha \cdot [b(f_0,\hat{f}_0)]^\beta \cdot [c(f_0,\hat{f}_0)]^\gamma,$$

where $a(f_0,\hat{f}_0) = \frac{2\mu_{f_0}\mu_{\hat{f}_0}+C_1}{\mu_{f_0}^2+\mu_{\hat{f}_0}^2+C_1}$, $b(f_0,\hat{f}_0) = \frac{2\sigma_{f_0}\sigma_{\hat{f}_0}+C_2}{\sigma_{f_0}^2+\sigma_{\hat{f}_0}^2+C_2}$ and $c(f_0,\hat{f}_0) = \frac{\sigma_{f_0\hat{f}_0}+C_3}{\sigma_{f_0}\sigma_{\hat{f}_0}+C_3}$, μ_{f_0} and σ_{f_0} are the local mean and standard deviation for f_0, and $\sigma_{f_0\hat{f}_0}$ is the cross-covariance of $\hat{f}_0$ and f_0. As suggested in [36] , we set $\alpha = 1$, $\beta = 1$ and $\gamma = 1$, $C_1 = (0.01L)^2$, $C_2 = (0.03L)^2$, and $C_3 = C_2/2$, where L is a specified dynamic range value of the input image.

Figure 4 shows the PSNR and SSIM values for the noisy simulated cases under different noise intensity levels. The PSNR and SSIM values are averaged over ten replicated experiments to reduce the random effect of noise generation. To ease the comparison, we also computed the PSNR and SSIM rank scores of the compared methods. The rank score of a method for each performance metric was computed as a sum of all the ranks among the compared methods over four test images, and lower average rank values implies better ranked. Table 1 show the PSNR rank scores and SSIM rank scores. The rank scores vary depending on the noise intensity P, but the overall performance of the sFBP is better than the other compared methods. Figures S1 and S2 in the

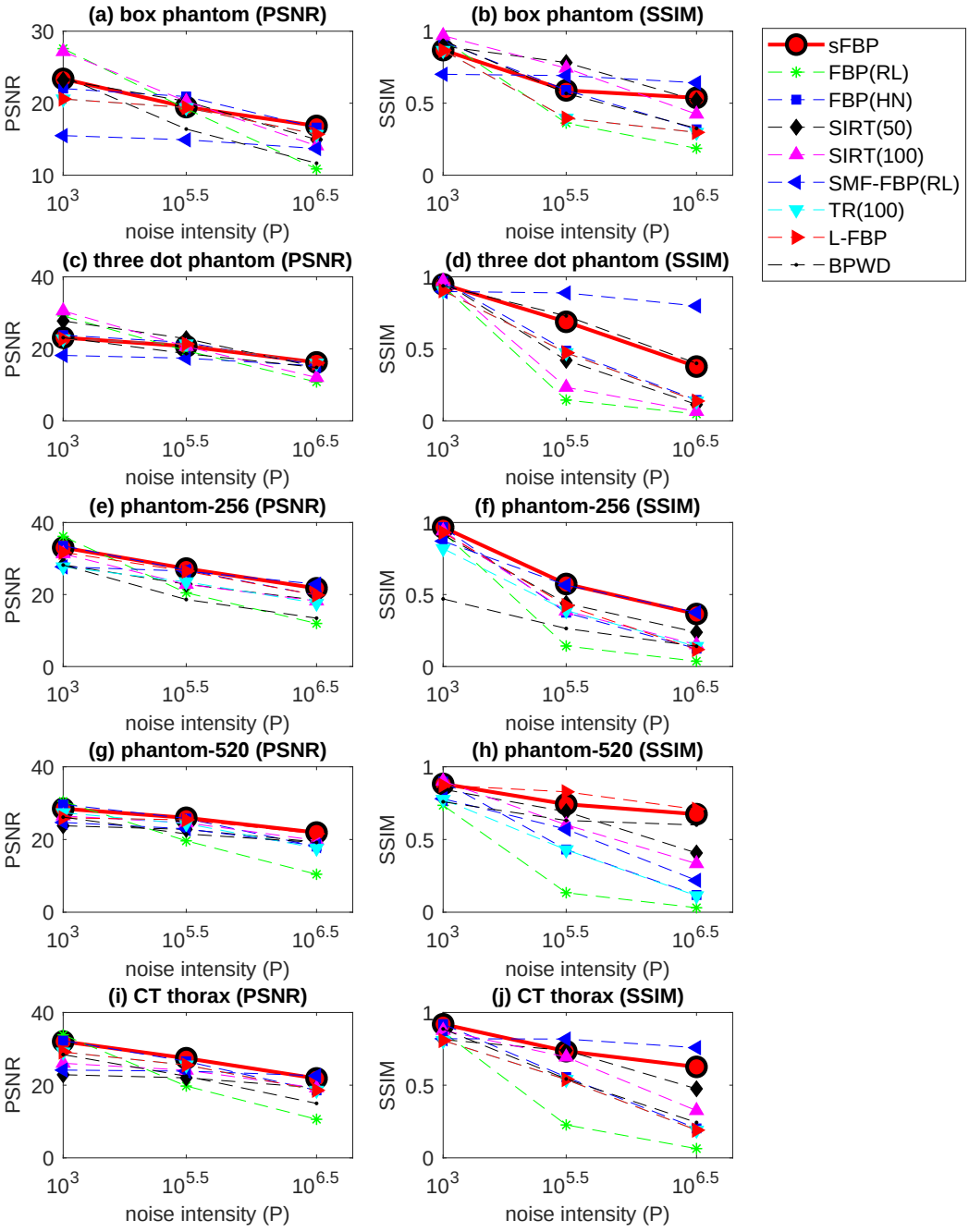

Figure 4: PSNR and SSIM of reconstructions for noisy simulated cases.

supplemental material illustrate the outcomes of all the compared methods for qualitative comparison. Details of the individual comparison and discussion are described below.

Noise Intensity	10^3	$10^{5.5}$	$10^{6.5}$
sFBP	19	12	7
FBP(RL)	6	40	45
FBP(HN)	16	9	24
SIRT(50)	32	25	23
SIRT(100)	20	24	27
TR(100)	31	21	25
L-FBP	32	21	18
SMF-FBP	42	33	20
BPWD	27	40	36

(a) PSNR

Noise Intensity	10^3	$10^{5.5}$	$10^{6.5}$
sFBP	17	14	11
FBP(RL)	27	45	45
FBP(HN)	11	27	30
SIRT(50)	25	16	20
SIRT(100)	10	25	25
TR(100)	37	32	33
L-FBP	33	27	31
SMF-FBP	37	13	10
BPWD	28	26	20

(b) SSIM

Table 1: Rank scores of the compared methods for different noise intensity levels. Panel (a) contains the rank scores with respect to PSNR, and panel (b) contains the rank scores with respect to SSIM.

Comparison to FBP. The FBP(RL) worked very well for the lowest noise intensity level, but it did not work well for higher noise cases, and changing the filter to Hann filter, resulting in FBP(HN), made significant improvement in both PSNR and SSIM. The proposed method, sFBP, worked better than FBP(HN), which justifies the need of the filter optimization proposed in sFBP. The computation times of the two FBP methods and sFBP were comparable, faster than the other competing methods.

Comparison to SIRT and TR. Both of the SIRT and TR are algebraic

iterative methods, where the TR basically introduces the generalized Tikhonov regularization to modify the SIRT iterations. The SIRT(100) worked better than the SIRT(50) for the lowest noise case with $P = 10^3$, while the result was opposite for the highest noise case with $P = 10^{6.5}$. Please note that the number of iterations typically determines how much detailed features are included in the resulting reconstruction. For the lowest noise case, more iterations would improve the reconstruction accuracy. However, for the highest noise case, more iterations also imply the overfit of the reconstruction to noises, which is also observed in other literature [17]. The TR method worked comparably to SIRT(50).

Comparison to L-FBP. The L-FBP is a filter optimization approach that improves the performance of FBP comparably to the algebraic iterative algorithm and runs as fast as the FBP. It has a tuning parameter, k, which controls noise in the reconstruction. In general, large k gives more noisy reconstruction but keeps fine details of image features, while smaller k has opposite effects. We chose $k = 10000$, which gave best PSNR among the values ranging in 20 to 10000. For the high noise case, the L-FBP performed better than both of FBP(RL) and FBP(HN), but the proposed sFBP method worked better than the L-FBP.

Comparison to SMF-FBP. The SMF-FBP [33] is a sinogram denoising technique that mainly applies a special mean filter on sinogram for denoising and then perform the conventional filtered backprojection on the denoised data. The SMF-FBP performed very well for the high noise case as competitive as the proposed sFBP. However, its performance was not very good for the low and medium noise cases, because it produces undesirable artifact. For the first test image, the SMF-FBP produces two white vertical lines that do not exist in the original image and therefore the PSNR and SSIM are relatively low. For the second image, it produces circular line patterns.

Comparison to BPWD. The BPWD [34] applies a deconvolution with Wiener

filter after the standard backprojection to get the reconstruction. The BPWD method is a backprojection-and-then-filtering method, as it performs backprojection first then applies deconvolution, by the convolution theorem that a pointwise multiplication in the frequency domain corresponds to a convolution in the spatial domain. The backprojection is a convolution of the target image and the point spread function (PSF) and the Wiener filter is a pseudo-inverse filter of the PSF in the frequency domain. The BPWD method then applies deconvolution for the backprojection with the Wiener filter to acquire the estimated target image (reconstruction). Also, as verified in the paper, the Wiener filter has some denoising ability. In [34], a new weighted ramp filter is also used in calculating the PSF. The proposed weighted ramp filter is expressed as $W = (\alpha M + 1)|R|$, where R is the ramp filter, M is a normalized weight matrix for real projections and α is the weights relative to interpolated samples. In our implementation of the algorithm on the testing images in this paper, we use the parameter $\alpha = 80$. The new weighted ramp filter is said to work well for sparse projections available. Also, what worth mentioning is that this method uses Wiener filter, which is good for white noise rather than Poisson noise and the method can perform better for large CT images. The BPWD method can produce good reconstruction but the reconstruction is still noisy for high level of noise and it has some blurring on the edges when looking at the details of the reconstruction.

3. SIRT + sFBP: Sparse Filtered SIRT (sfSIRT)

In most electron tomography experiments, it is often difficult to obtain 2D sinograms for a full range of 180 degree tilt angles, and the accessible tilt angles typically range from -65 (or 75) degrees to +65 (or +75) degrees for electron tomography experiments. Since many tomography construction approaches were developed assuming that sinogram data are available for a full angular range (i.e. $[-90, 90]$ degrees), applying the approaches with limited angles could create some image artifacts in the resulting reconstruction, which is known as the missing wedge effect. According to our numerical experiments, most of the

advanced FBP methods including our sFBP suffers from the missing wedge effect up to different degrees. To mitigate the missing wedge effect in sFBP, we propose to combine sFBP with the simultaneous iterative reconstruction method. This section describes the idea of integrating sFBP and SIRT and presents its numerical performance.

The SIRT algorithm updates its tomographic reconstruction iteratively until the backprojection of its latest reconstruction reaches close to the input projection data. Let $f^{(k)}$ denote the reconstruction achieved at the kth iteration of SIRT and let p represents the input sinogram. The $(k+1)$th iteration involves the update,

$$f^{(k+1)} = f^{(k)} + \lambda \mathcal{A}^T (p - \mathcal{A} f^{(k)}),$$

where $\mathcal{A}$ represents the Radon transformation, and $\mathcal{A}^T$ represents the backprojection. The iteration basically takes the projection image of the kth reconstruction outcome, evaluates its deviation from the input projection data, and finally uses the deviation to improve the reconstruction outcome [2]. Observed from our experiments in Section 2.3 as well as other literature [17], the SIRT iteration tends to overfit the observation noises contained in the input sinogram as k increases. Therefore, the determination of an appropriate iteration number is important, but there is no good rule of thumb for determining it. To mitigate the overfit issue, Wolf et al. [37] proposed to replace the backprojection operator $\mathcal{A}^T$ with a filtered backprojection using a low-pass filter, which we refer to as the filtered SIRT (fSIRT) in this paper. Motivated by the same idea, we propose to replace the backprojection operator $\mathcal{A}^T$ with our sFBP which has greater denoising capabilities than the existing FBP methods as shown in Section 2.3. We also use a stopping criteria of the iteration to avoid unnecessarily long iterations and consequently reduce the computation time for reconstruction. We stop the iteration if the following convergence criteria is met,

$$|f^{(k+1)} - f^{(k)}| \leq \epsilon. \tag{16}$$

The SIRT iteration with the new filtered backprojection is referred to as 'Sparse

Filtered SIRT (sfSIRT)'. We conjecture that the proposed method converges faster than the standard SIRT, because sFBP regularizes the backprojection operation, so the resulting reconstruction outcome is less fluctuating. The faster convergence implies a less number of the iterations required until convergence so a less computation time. We will use numerical examples to show this in the next subsection.

3.1. Reconstruction Accuracy for Limited Angle Scenarios

For a numerical study, we emulated multiple limited angle scenarios with different choices of tilt angle ranges $(-r, r)$, while fixing the Poisson noise intensity at $P = 10^{5.5}$. We varied $r \in \{65, 70, 75, 80, 85, 90\}$. For each choice of r, sinogram data was generated for each integer-valued tilt angle belonging to the interval $(-r, r)$, following the same data generation procedure in Section 2.3. The sinogram data were used as an input to the compared methods, which include sFBP, FBP, SIRT, fSIRT, L-FBP, TR, BPWD, and sfSIRT (our method). For FBP, L-FBP and fSIRT, we applied the Cosine filter instead of the Hann filter and the Ram-Lak filter, because the Cosine filter produced better results in our numerical trials. For SIRT, sfSIRT, fSIRT and TR, the maximum number of iterations performed is 100; the iteration may stop earlier because we applied the stopping criterion (16). The PSNR and SSIM measures of the methods were measured for 10 replicated simulation cases, and the measures were averaged over the replications.

The PSNR and SSIM performances of the methods are summarized in Figure 5. In terms of PSNR, our proposed method (sfSIRT) outperformed the other competing methods for most of the experimental settings, and the proposed method was consistently the top three performers in terms of SSIM. In particular, sfSIRT performed better than sFBP significantly (a non-iterative version of our proposed method), which was performed worse than SIRT for limited angle scenarios. This says that iteratively applying sFBP within SIRT is quite effective in mitigating the missing wedge effect. In addition, sfSIRT uniformly outper-

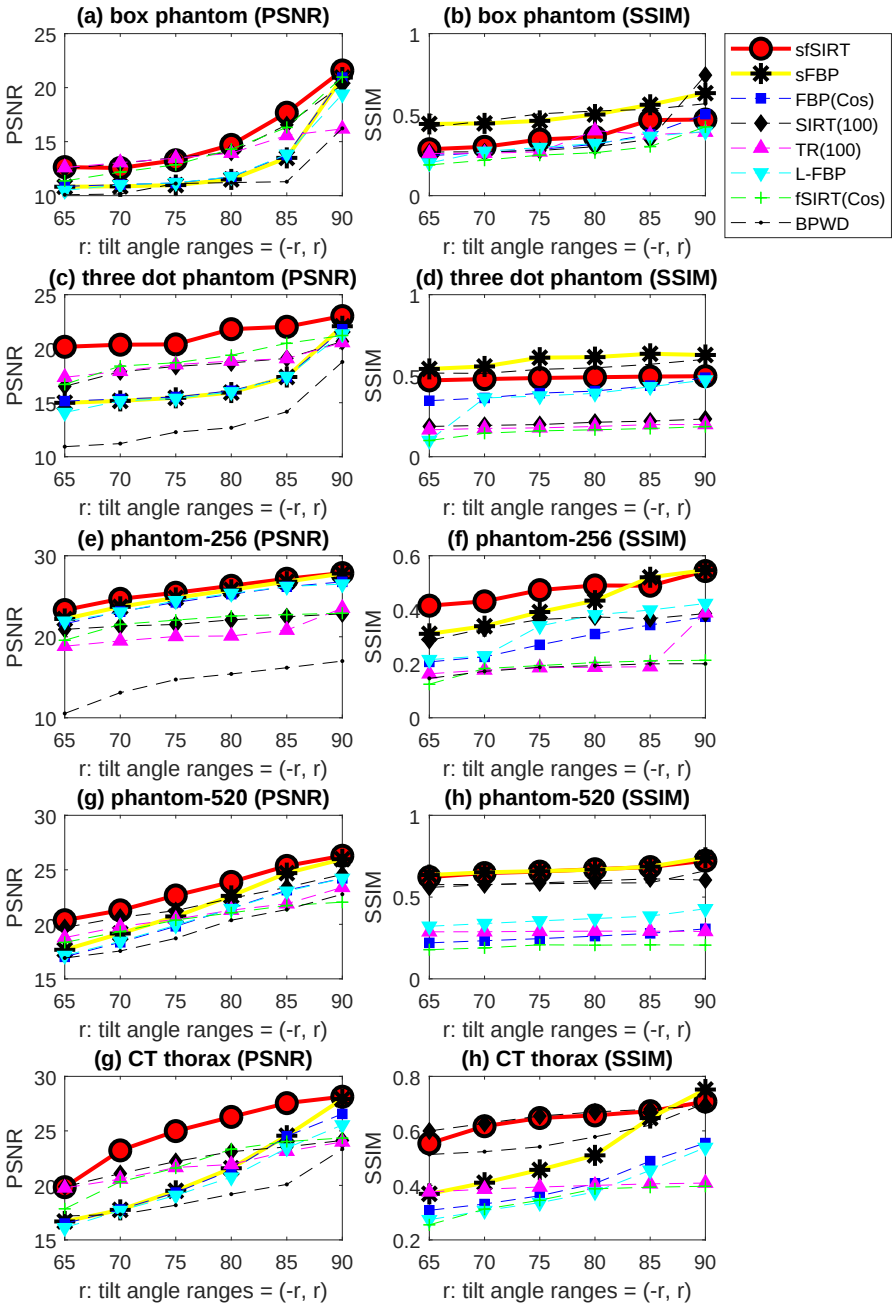

Figure 5: PSNR and SSIM of reconstructions for different ranges of available tilt angles.

Methods	Time (seconds)	# of iterations to stop
SIRT with stopping condition	26.1231	20.0
fSIRT with stopping condition	Do not converge	N.A.
sfSIRT with stopping condition	11.54	8.4
sFBP	2.12808	N.A.
L-FBP	2.20	N.A.
SMF-FBP	5.73	N.A.
BPWD	3.02	N.A.

Table 2: Average computation times (seconds) and the average number of iterations run under $P = 10^{5.5}$ and $r = 65$ for the fourth test image.

formed SIRT in PSNR, which implies that introducing the proposed sFBP in SIRT iterations gives additional performance gains over SIRT. For qualitative comparison, we present the reconstruction outcomes of sfSIRT, fSIRT, SIRT and sFBP in Figure S3 of the supplementary material. The proposed method reduces the image artifacts due to the missing wedge. For example with the three dot phantom image, the white spots below the three dots were the image artifacts, and the sfSIRT reduced the artifacts significantly. The sfSIRT is still limited to the box phantom image, but this is the same for all compared methods.

3.2. Comparison of Computation Time

In this section, we compare the computational costs of three iterative tomography reconstruction methods, SIRT, fSIRT and our proposed sfSIRT. Since their computation costs per iteration are comparable, the computation costs of the three methods largely depend on the number of the iterations run, which are determined by how fast the iterative methods converge. We compare the computation times and convergence behaviors of the three methods.

For the comparison, we use the fourth test image, thorax CT image, as bench-

mark data, and ten noisy sinograms of the benchmark image were simulated using the same way that we used in the previous section with the settings $P = 10^{5.5}$ and $r = 65$. We applied the stopping criterion (16) for all of the three iterative methods. Table 2 summarizes the average number of iterations run and the corresponding computation times on average. The sfSIRT has converged faster that SIRT; the sfSIRT converged in 8.4 iterations on average, while SIRT converged in 20 iterations. The reason for the faster convergence of the sfSIRT can be explained by its use of sFBP as the backprojection operator in the SIRT iteration. The sFBP optimizes its backprojection filter with some regularization, and accordingly the iteration outcome of sfSIRT is regularized. This regularization on the solution path over iterations leads to the overall faster convergence for sfSIRT, while there is no such regularization on SIRT.

To look at the convergence behavior of the three method, we plotted the stopping criterion values over iterations in Figure 6-(a). The stopping criterion for sfSIRT decreases faster than those for the other two methods, and the value actually diverged for fSIRT. We also looked at how the stopping criterion is related to PSNR values in Figure 6-(b), (c) and (d). For both of sfSIRT and SIRT, PSNR values were inversely correlated to the stopping criterion. This implies that stopping at lower stopping criterion would give better PSNR performance, so the choice of the stopping criterion gives a reasonable guidance to acquire a better reconstruction. However, for fSIRT, the correlation was random, so the stopping criterion does not really give a good guide to the reconstruction accuracy, which may limit the applicability of fSIRT.

4. Real Data Examples: Tomographic Reconstruction of Nanoparticles

In this section, we present the application of the proposed method for tomographic imaging of nanoparticles. Nanoparticles are ultrafine particles whose dimensions are less than 100 nanometers. The properties of nanoparticles are

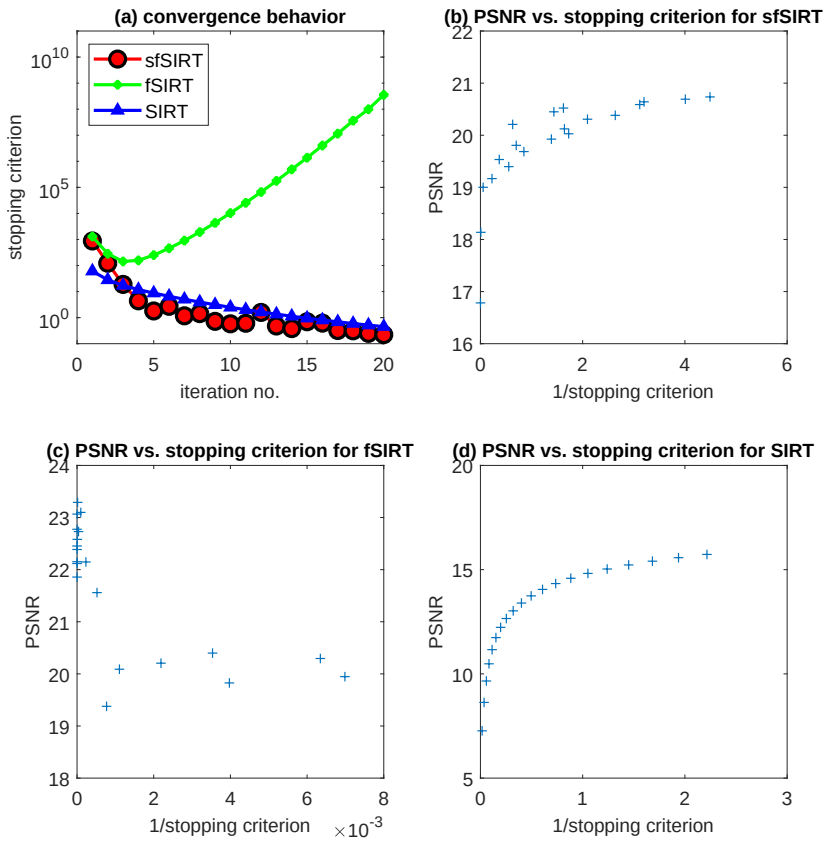

Figure 6: Convergence Behavior of sfSIRT (our method), fSIRT (with Cosine filter) and SIRT.

determined by the shapes and sizes of the nanoparticles, so quantifying the particle sizes and shapes is one of the essential steps to perform after the synthesis of nanoparticles [38]. In many material research, the quantification has been mostly performed using two-dimensional images of nanoparticles, because a conventional transmission electron microscope only gives a two-dimensional projection image of three-dimensional nanoparticles. With a tomography tilt sample holder [39], one can achieve the two-dimensional projection images from multiple projection angles. However, combining the tilt series of the project images into a three dimensional image is still challenging due to the missing

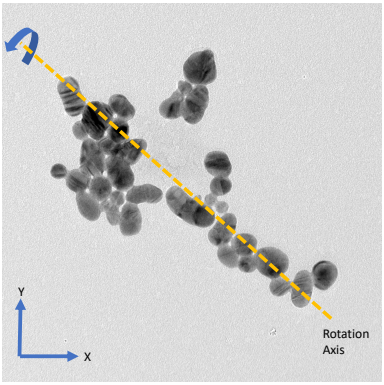

Figure 7: 64th projection image of the gold nanoparticle tomography data. As we can see from the 3D reconstruction, the rotation axis is along the NP chain. The parallel beam direction (z-direction) is orthogonal to the projection image direction.

wedge issue and image noises. We demonstrate the capability of our method for achieving the three dimensional image of nanoparticles. In this section, we use two data sets of electron tomography images of different nanoparticles to illustrate our method with comparison to the other approaches compared in the previous section.

4.1. Real Data Set 1: A Chain of Gold Nanoparticles

We apply sfSIRT, sFBP, SIRT and fSIRT with Cosine filter to electron tomography images we took for a sample of gold nanoparticles. The images consist of the projections from 103 different tilt angles in between $-65°$ to $65°$, in which from $-65°$ to $0°$ we get the one projection image roughly per $2°$ and from $0°$ to $65°$ we get the one projection image roughly per $1°$. Tomographic tilt-series were acquired manually using SerialEM [39] on a JEOL-ARM200cF cold field emission microscope operated at 200kV. A Fischione tomography holder was used, which can tilt up to 90 degrees. The images were obtained using a Gatan Orius 2k by 2k camera. As an example, the 64th projection image is shown in Figure 7. As we can see from the 3D reconstruction following, the rotation axis is along the NP chain. Each image was taken with a pixel size

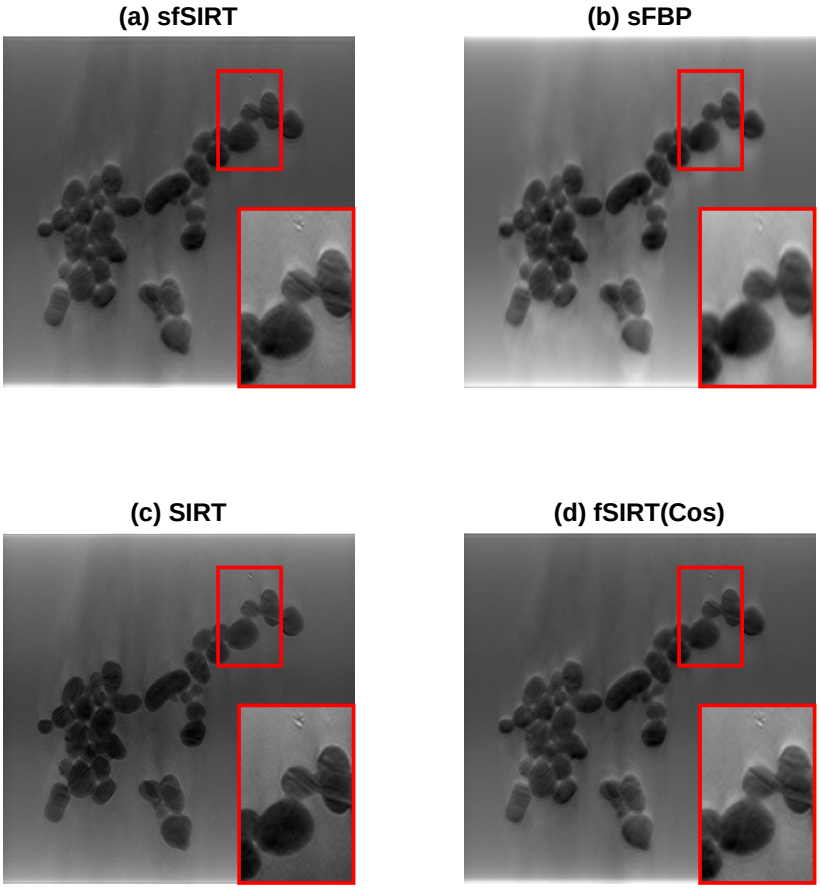

Figure 8: 3D reconstructions results from the gold NP tomographic reconstructions from (a) sfSIRT (b) sFBP (c) SIRT (d) fSIRT with Cosine filter. The reconstruction viewed through x-y plan was shown, and each sub-figure comes with a partial magnification of the sub-figure on its bottom right.

0.13 nm by 0.13 nm and an acquisition time of 1 second. We used Etomo from IMOD [40] in doing the alignment of the raw TEM projection images. For tomography reconstruction, we used the 'reconstruction-and-stacking' method as we described in Section 2, which reconstructs the 2D slices of a tomogram independently using the corresponding slices of sinograms.

The results of the 3D reconstructions are shown in Figure 8. Each sub-figure

presents the 3D reconstruction viewed through the $(x, y)-$plane, which comes with the magnified image of a part of the reconstruction. For this dataset, the image artifact due to the missing wedge is the white spots widely spread around actual gold nanoparticles (shown as dark-colored) along the y-direction. The sfSIRT reduces the white spots significantly.

4.2. Real Data Set 2: A Single Platinum Nanoparticle

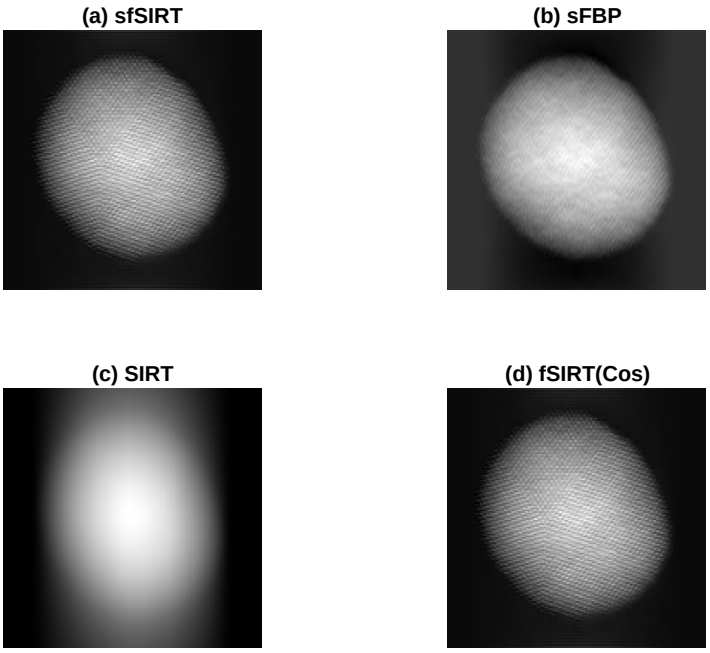

Figure 9: 3D reconstructions results from single platinum NP tomographic reconstructions from (a) sfSIRT (b) sFBP (c) SIRT (d) fSIRT with Cosine filter. The reconstruction viewed through x-y plan was shown.

We apply sfSIRT, sFBP, SIRT and fSIRT with Cosine filter to 2D projection images of a single platinum nanoparticle, which are available in the literature [41]. For more details on the dataset, we refer to the original article. We used 80 projection images acquired with the tomography tilt angles ranging from $-72.6°$ to $72.6°$ with equal increments. The results of the 3D reconstructions are shown in Figure 9. The sFBP method has shown some image artifacts due

to the missing wedge, which correspond to the white spots spread in the left side and right side of the platinum nanoparticle along the x-direction, while SIRT produces a very blurred reconstruction. Both of fSIRT and sfSIRT preserve the detailed structures at an atomic resolution very well.

5. Conclusion

In this paper, we present a novel filter-optimization approach to improve the filtered backprojection (FBP) for tomographic reconstruction. The new approach, sFBP, formulates an optimization problem that optimizes the backprojection filter to minimize a regularized reconstruction error. The optimal solution of the optimization formulation can be achieved by applying a simple thresholding rule on the one-dimensional Fourier transform of sinogram data. This simple solution approach makes the computation of sFBP is as fast as that of the conventional FBP. In many numerical examples with simulated noisy sinogram, the approach has shown the greater trade-offs between the reconstruction accuracy and the computation efficiency than other existing methods. In particular, its reconstruction accuracy for higher noise cases was superior to the compared methods.

We also proposed the use of sFBP as a plug-in backprojection operator within the simultaneous iterative reconstruction technique (SIRT), which significantly improved the reconstruction accuracy over sFBP and SIRT when sinogram data are only available for a limited range of projection angles (or holder tilt angles in electron tomography). The computation time for the SIRT combined with sFBP, which we refer to as 'sfSIRT', is in between those of sFBP and SIRT. It spends more computation time than sFBP, because sfSIRT needs to repeat sFBP multiple times to iteratively update its reconstruction. On the other hand, sfSIRT spends much less computation time than the conventional SIRT, because the sfSIRT's iteration converges faster than the SIRT iteration. We believe the proposed approach would be very practical with those strengths. The general

idea has be easily generalized and modified to three-dimension tomographic reconstruction problems, which was shown using two real data examples in 3D electron tomography.

Supplementary Material

This paper contains one supplementary material which contains three large figures. Figures S1 and S2 contains the reconstruction results for the numerical study in Section 2.3, and Figure S3 contains the reconstruction results for the numerical study in Section 3.1.

Acknowledgment

This work is partially supported by AFOSR FA9550-18-1-0144. The TEM work was performed at the National High Magnetic Field Laboratory, which is supported by NSF DMR-1157490 and the State of Florida.

References

[1] H. Jinnai, R. J. Spontak, Transmission electron microtomography in polymer research, Polymer 50 (2009) 1067–1087.

[2] A. Kak, M. Slaney, Principles of computerized tomographic imaging, Society of Industrial and Applied Mathematics, Philadelphia, PA, USA, 2001.

[3] X. Pan, E. Y. Sidky, M. Vannier, Why do commercial CT scanners still employ traditional, filtered back-projection for image reconstruction?, Inverse Problems 25 (12) (2009) 421–434.

[4] V. Gesù, G. Bosco, F. Millonzi, C. Valenti, A memetic approach to discrete tomography from noisy projections, Pattern Recognition 43 (9) (2010) 3073–3082.

[5] R. Gordon, R. Bender, G. T. Herman, Algebraic reconstruction techniques (ART) for three-dimensional electron microscopy and x-ray photography, Journal of Theoretical Biology 29 (3) (1970) 471–481.

[6] G. T. Herman, Image Reconstruction from Projections: The Fundamentals of Computerized Tomography, Academic Press, New York, NY, USA, 1980.

[7] A. H. Andersen, A. C. Kak, Simultaneous algebraic reconstruction technique (SART): A superior implementation of the art algorithm, Ultrason Imaging 6 (1984) 81–94.

[8] X. Lu, Y. Sun, Y. Yuan, Optimization for limited angle tomography in medical image processing, Pattern Recognition 44 (10–11) (2011) 2427–2435.

[9] M. Vauhkonen, D. Vadász, P. A. Karjalainen, E. Somersalo, J. P. Kaipio, Tikhonov regularization and prior information in electrical impedance tomography, IEEE Transactions on Medical Imaging 17 (2) (1998) 285–293.

[10] J. L. Mueller, S. Siltanen, Linear and Nonlinear Inverse Problems with Practical Applications, SIAM, 2012.

[11] D. Yu, J. Fessler, Edge-preserving tomographic reconstruction with nonlocal regularization, IEEE Transactions on Medical Imaging 21 (2) (2002) 159–173.

[12] L. A. Flores, V. Vidal, P. Mayo, F. Rodenas, G. Verdú, CT image reconstruction based on GPUs, Procedia Computer Science 18 (2013) 1412–1420.

[13] F. Xu, K. Mueller, Accelerating popular tomographic reconstruction algorithms on commodity pc graphics hardware, IEEE Transactions on Nuclear Science 52 (3) (2005) 654–663.

[14] Z. Ren, G. Liu, Z. Huang, Study on an improved filtered back-projection image reconstruction algorithm combined with wavelet denoising, in: International Symposium on Photoelectronic Detection and Imaging 2013:

Infrared Imaging and Applications, Vol. 8907, International Society for Optics and Photonics, 2013, p. 890710.

[15] D. Karimi, P. Deman, R. Ward, N. Ford, A sinogram denoising algorithm for low-dose computed tomography, BMC Medical Imaging 16 (11) (2016) 1–14.

[16] J. Wang, T. Li, H. Lu, Z. Liang, Penalized weighted least-squares approach to sinogram noise reduction and image reconstruction for low-dose x-ray computed tomography, IEEE Transactions on Medical Imaging 25 (10).

[17] L. G. Zeng, A filtered backprojection algorithm with characteristics of the iterative landweber algorithm, Medical Physics 39 (2) (2012) 603–606.

[18] L. G. Zeng, A filtered backprojection map algorithm with non-uniform sampling and noise modeling, Medical Physics 39 (4) (2012) 2170–2178.

[19] L. G. Zeng, A. Zamyatin, A filtered backprojection algorithm with ray-by-ray noise weighting, Medical Physics 40 (3) (2013) 031113:1–7.

[20] D. M. Pelt, K. J. Batenburg, Improving filtered backprojection reconstruction by data-dependent filtering, IEEE Transactions on Image Processing 23 (11) (2014) 4750–4762.

[21] D. M. Pelt, K. J. Batenburg, Accurately approximating algebraic tomographic reconstruction by filtered backprojection, in: Proceedings of The 13th International Meeting on Fully Three-Dimensional Image Reconstruction in Radiology and Nuclear Medicine, Newport, Rhode Island, USA, 2015, pp. 158–161.

[22] T. Lukića, P. Balázsb, Binary tomography reconstruction based on shape orientation, Pattern Recognition Letters 79 (2016) 18–24.

[23] B. Cheikh, E. Baudrier, G. Frey, A tomographical reconstruction method from unknown direction projections for 2d gray-level images, Pattern Recognition Letters 85 (2017) 49–55.

[24] T. Wang, T. Sze, The image moment method for the limited range ct image reconstruction and pattern recognition, Pattern Recognition 34 (11) (2001) 2145–2154.

[25] H. Shu, J. Zhou, G. Han, L. Luo, J.Coatrieux, Image reconstruction from limited range projections using orthogonal moments, Pattern Recognition 40 (2) (2007) 670–680.

[26] X. Dai, H. Shu, L. Luo, G. Han, J.Coatrieux, Reconstruction of tomographic images from limited range projections using discrete radon transform and tchebichef moments, Pattern Recognition 43 (3) (2010) 1152–1164.

[27] E. Acar, S. Peltonen, U. Ruotsalainen, Adaptive multiresolution method for MAP reconstruction in electron tomography, Ultramicroscopy 170 (2016) 24–34.

[28] K. P. Burnham, D. R. Anderson, Model Selection and Multimodel Inference: A Practical Information-Theoretic Approach, 2nd Edition, Springer, New York, NY, USA, 2002.

[29] H. Akaike, A new look at the statistical model identification, IEEE Transactions on Automatic Control 19 (6) (1974) 716–723.

[30] G. E. Schwarz, Estimating the dimension of a model, Annals of Statistics 6 (2) (1978) 461–464.

[31] M. H. Hansen, B. Yu, Model selection and minimum description length principle, Journal of American Statistical Association 96 (2001) 746–774.

[32] P. Bühlmann, B. Yu, Sparse boosting, Journal of Machine Learning Research 7 (2006) 1001–1024.

[33] H. Qu, F. Xu, X. Hu, L. Wang, J. Zhao, Z. Zhang, A novel denoising method based on radon transform and filtered back-projection reconstruction algorithm, Optics and Lasers in Engineering 50 (4) (2012) 593–598.

[34] Z. Wang, J. Cai, W. Guo, M. Donnelley, D. Parsons, I. Lee, Backprojection wiener deconvolution for computed tomographic reconstruction, PloS one 13 (12) (2018) e0207907.

[35] Patient information and CT scan, accessed: 2018-07-30.
URL http://users.telenet.be/alain.dens/Patient_info_CT_nl.html

[36] Z. Wang, A. C. Bovik, H. R. Sheikh, E. P. Simoncelli, Image quality assessment: From error visibility to structural similarity, IEEE Transactions on Image Processing 13 (4) (2004) 600–612.

[37] D. Wolf, A. Lubk, H. Lichte, Weighted simultaneous iterative reconstruction technique for single-axis tomography, Ultramicroscopy 136 (2014) 15–25.

[38] K. L. Kelly, E. Coronado, L. L. Zhao, G. C. Schatz, The optical properties of metal nanoparticles: The influence of size, shape, and dielectric environment, The Journal of Physical Chemistry B 107 (3) (2003) 668–677.

[39] D. Mastronarde, Automated electron microscope tomography using robust prediction of specimen movements, Journal of Structural Biology 152 (2005) 36–51.

[40] J. R. Kremer, D. N. Mastronarde, J. R. McIntosh, Computer visualization of three-dimensional image data using imod, Journal of Structural Biology 116 (1) (1996) 71–76.

[41] B. D. A. Levin, E. Padgett, C.-C. Chen, M. C. Scott, R. Xu, W. Theis, Y. Jiang, Y. Yang, C. Ophus, H. Zhang, D.-H. Ha, D. Wang, J. Yu, H. D. Abrũna, R. D. Robinson, P. Ercius, L. F. Kourkoutis, J. Miao, D. A. Muller, R. Hovden, Nanomaterial datasets to advance tomography in scanning transmission electron microscopy, Scientific Data 3 (160041).